Global increases of salt intrusion in estuaries under future environmental conditions

Lee, Jiyong; Biemond, Bouke; van Keulen, Daan; Huismans, Ymkje; van Westen, René M.; de Swart, Huib E.; Dijkstra, Henk A.; Kranenburg, Wouter M.

Important note
To cite this publication, please use the final published version (if applicable).
Please check the document version above.

Article

Global increases of salt intrusion in estuaries under future environmental conditions

Jiyong Lee [1] ✉, Bouke Biemond[1], Daan van Keulen[2,3], Ymkje Huismans[2,4], René M. van Westen [1], Huib E. de Swart[1], Henk A. Dijkstra[1,5] & Wouter M. Kranenburg [2,4]

In recent years, increased salt intrusion in surface waters has threatened freshwater availability in coastal regions worldwide. Yet, current future projections of salt intrusion are limited to local regions or changes to single forcing agents. Here, we quantify compounding contributions from changes in river discharge and relative sea level to changing future salt intrusion under a high-emission scenario (Shared Socioeconomic Pathway, SSP3-7.0) for 18 estuaries around the world. We find that the annual 90th percentile future salt intrusion is projected to increase between 1.3% and 18.2% (median 9.1%) in 89% of the studied estuaries worldwide. Our analysis also indicates that, on average, sea-level rise contributes approximately two times more to increasing future salt intrusion than reduced river discharge. We further show that the return levels of present-day 100-year salt intrusion events are projected to increase between 3.2% and 25.2% (median 10.2%) in 83% of the studied estuaries.

Estuaries are semi-enclosed bodies of water, where saline ocean and fresh river water meet and mix. Estuaries are considered as highly important socioeconomic areas due to their geological and ecological benefit. Approximately 69% of large cities in the world (22 out of the 32 largest cities) are situated on estuaries[1]. In recent years, there have been reports about severe salt intrusion events around the world. The US Army Corps of Engineers (USACE) constructed an emergency sill to impede salt intrusion invading the Mississippi River, when New Orleans' municipal drinking water sources were predicted to be contaminated during the city's 132-year historical record drought over the summer and fall of 2023[2]. Similarly, two severe drought events occurred in the Rhine-Meuse Estuary (the Netherlands) in 2018 and 2022, which caused prolonged salt intrusion impacting the freshwater intakes. In 2018, chloride concentration exceeded twice the drinking water norm for 75 consecutive days at the river mouth of the Hollandsche IJssel (the Netherlands) - a strategic river branch for fresh water intake. Except for the year 2018, such severe salt intrusion events only occured 52 days in the decade (2011–2020)[3].

Many climate studies have demonstrated that, by the end of the 21st century, droughts are projected to increase in frequency, and their intensity is expected to be enhanced in many regions[4–6]. In addition, sea-level rise (SLR) in future climates is also projected to deepen estuaries[7]. Reduced river discharge decreases export of salt, while SLR enhances salt import by strengthening estuarine circulation and reducing river flow velocity[8,9]. Increasing water depth due to SLR can alter tidal amplitudes in coastal regions[10], with varying effects on salinity depending on estuarine regimes[11]. In stratified estuaries (exchange flow dominant regime), larger tidal amplitudes weaken estuarine circulation, reducing salt intrusion. Conversely, in well-mixed estuaries (tidal dispersion dominant regime), higher tidal amplitudes enhance tidal dispersion, increasing salt intrusion. Increased ocean salinity imposes stronger baroclinic pressure and allow saline water to intrude further inland[12]. Enhanced ocean surface stress, driven by wind blowing from the sea toward land, can also amplify estuarine circulation and salt intrusion[13]. Among these modulations in estuarine dynamics, reduced river discharge and rising

[1]Department of Physics, Institute for Marine and Atmospheric Research Utrecht (IMAU), Utrecht University, Utrecht, The Netherlands. [2]Deltares, Delft, The Netherlands. [3]Hydrology and Environmental Hydraulics, Wageningen University & Research, Wageningen, The Netherlands. [4]Department of Hydraulic Engineering, Delft University of Technology, Delft, The Netherlands. [5]Department of Civil, Environmental and Mechanical Engineering, University of Trento, Trento, Italy. ✉e-mail: leej6@ornl.gov

water depth due to SLR have been considered as two dominant processes responsible for increasing salt intrusion length in the future[14]. Here, salt intrusion length is defined as the distance from the mouth to a location where bottom salinity equals to 2 psu. The salt intrusion length is of great interest for multiple stakeholders since it limits water supplies[15], and affects biodiversity[16] and crop yields[17].

The potential risk of enhanced salt intrusion under climate change has been quantified using numerical modeling studies[7,14,18–24]. However, most previous works mainly focused on changes in only one forcing agent: either river discharge[18] or SLR[7,19–21]. This poses challenges in providing a comprehensive understanding of climate change effects on future salt intrusion and quantifying the contribution from each driver. Although studies exist that account for both future river discharge and SLR, these investigate only individual estuaries, and there is a lack of quantification on how climate change affects the statistical properties of future salt intrusion events[14,22–24].

Here, we determine relative changes in future salt intrusion length statistics, as compared to the present day, in 18 estuaries worldwide. The estuaries are selected based on the availability of data that is crucial for the current analysis: estuary geometries, salinity field data at different longitudinal positions, observed multi-year daily river discharge data, and reliable river discharge from a climate model. The estuaries included in this study are from the continents as follows: five (North America), one (South America), six (Europe), three (Africa), two (Asia), and one (Oceania). These sites are representative mid-latitude estuaries, where freshwater availability is expected to become critical issues in the coming decades due to increased salt intrusion driven by more frequent droughts and rising sea-level. All ranges of vertical salinity structures from stratified to partially mixed and well-mixed conditions, are observed in the chosen estuaries. The first aim of our study is to quantify the changes in the statistics of two forcing agents: river discharge and SLR. In this study, SLR consists of absolute and relative contributions. The absolute SLR (ASRL) is caused by steric expansion and the increased ocean volume from ice melt. The regional variability of ASRL was computed by considering gravitational, rotational, and deformational (GRD) effects and changes in the dynamic sea level. The relative SLR (RSLR) considers vertical land motion (VLM), which enables to quantify effective changes of water depth in estuaries. The second goal is to analyze changes in the salt intrusion length statistics due to changes in both forcing agents and how these responses depend on the properties of the considered estuaries. To this end, we obtained daily river discharge for the selected estuaries up to the year 2100 under the high emission scenario (SSP3-7.0) using Community Earth System Model 2 large ensemble simulation results (CESM-LE2, Methods and Supplementary Table S1). We applied a bias correction for the modeled daily river discharge from CESM-LE2 using observed river discharge data using the Quantile Delta Mapping (QDM)[25], see Supplementary Fig. S1 and Fig. S2. Next, we estimated projected regional ASLR due to increasing temperature by post-processing CESM-LE2 results following[26] (Methods). The VLM was also quantified for the selected estuaries to compute the RSLR, using data presented in ref. 27 (Methods). Thereafter, a tidally and width averaged, single channel surface water salt intrusion model was calibrated using salinity field measurements at different longitudinal locations (Methods, Supplementary Note S1). Three consecutive 35-year time windows are defined over the 21st century: present (1996–2030), intermediate future (2031–2065), and long-term future (2066–2100). Smooth transitions in river discharge and RSLR are observed between the intermediate and long-term future in the preliminary analysis. To save computational time, the calibrated salt intrusion model simulations were carried out only for the present (1996–2030) and long-term future (2066–2100) periods under four different combinations among dominant forcing agents: river discharge, ASLR, and VLM (Methods). Hereafter, the future period refers to the long-term future.

Results

River discharge projection

We first investigate the spatial variability of projected river discharge at the end of the 21st century. Figure 1a illustrates the relative changes in the 35-year mean of low discharge projected for the future period (2066–2100) compared to the present period (1996–2030). Here, low discharge is defined as the annual 10th percentile of the daily river discharge Q_{10}, which is a widely used drought index in hydrology[28,29]. The relative changes in low discharge correspond to $\Delta Q_{10}^* = (Q_{10}^f - Q_{10}^p)/Q_{10}^p$, where Q_{10}^p and Q_{10}^f are the time-averaged Q_{10} over the present and future periods, respectively. As seen, CESM-LE2 projects decreasing low discharge magnitude (red in Fig. 1a) in the southern part of North America, northern and southern parts of South America, western and southern Europe, West and South Africa, and some coastal regions of South East Asia, and the western and eastern parts of Australia. Conversely, the magnitude of low discharge is projected to increase (blue in Fig. 1a) along the east and west coasts of a northern part of North America, the middle east of South America, northern Europe, central and eastern Africa, some coastal regions of South East Asia, and central Australia. The projected river discharge by CESM-LE2 is mostly aligned with previous multi-model ensemble mean streamflow projections under the high emission scenario (Representative Concentration Pathway, RCP 8.5)[28,29]. However, the river discharge projections by CESM-LE2 for the west coast of the USA show the opposite direction of changes (increase) as compared to the multi-model ensemble mean in earlier studies (decrease). This difference is attributed to the fact that CESM branches (CESM1-BGC and CCSM4) show positive biases in future trends of river discharge under RCP 8.5 for these regions[30].

For the selected estuaries, quantification of relative changes in river discharge statistics (the 10th, 50th, and 90th percentiles, expressed by the different subscripts in ΔQ^*) are given in Fig. 1b. The considered river discharge indices are projected to increase consistently for most of the selected estuaries in North and South America. In addition, the estuaries in southern Europe and Africa show decreasing future river discharge indices. Some estuaries in western Europe and southern Africa also show opposite sign changes in extreme river discharge indices ($\Delta Q_{10}^* < 0$ and $\Delta Q_{90}^* > 0$), implying enhanced seasonality in a warming climate. The seasonally averaged 35-year mean river discharge are presented for the future and present periods in Supplementary Fig. S2, which supports the enhanced seasonality.

Relative sea-level rise (RSLR)

RSLR is determined from ASLR and VLM. The parameters δH_A and δH_{VLM} are defined as changes in water depth due to ASLR and VLM, respectively, and $\delta H_R = \delta H_A - \delta H_{VLM}$. We first quantify future projections of regional δH_A, including volume expansion of water column due to steric effects (Steric), ice melt (Glaciers, Greenland, and Antarctica), and changes in dynamic sea level (DSL) (Methods). A uniform increase of water level is assumed for the steric effect contribution. The GRD effects are considered for land ice melt (Supplementary Fig. S3). The GRD effects arise from the fact that ASLR is larger away from ice melting sources due to the reduced gravitational force that pulls the water surface. The contribution due to changes in DSL was also quantified, which was imposed by changes in regional wind stress and large-scale ocean circulation (Supplementary Fig. S4). Figure 2a shows the 35-year mean water surface elevation difference (δH_A) between the future and present-day periods. A dipole pattern of δH_A is found in the North Atlantic Ocean, which is associated with increased heat and fresh water fluxes, resulting in the weakening of the Atlantic Meridional Overturning Circulation (AMOC)[31,32].

To estimate increases in effective water depth in estuaries, we also considered regional VLM. We employed projected global coastal region VLM data from ref. 27, which utilizes GPS, satellite altimetry,
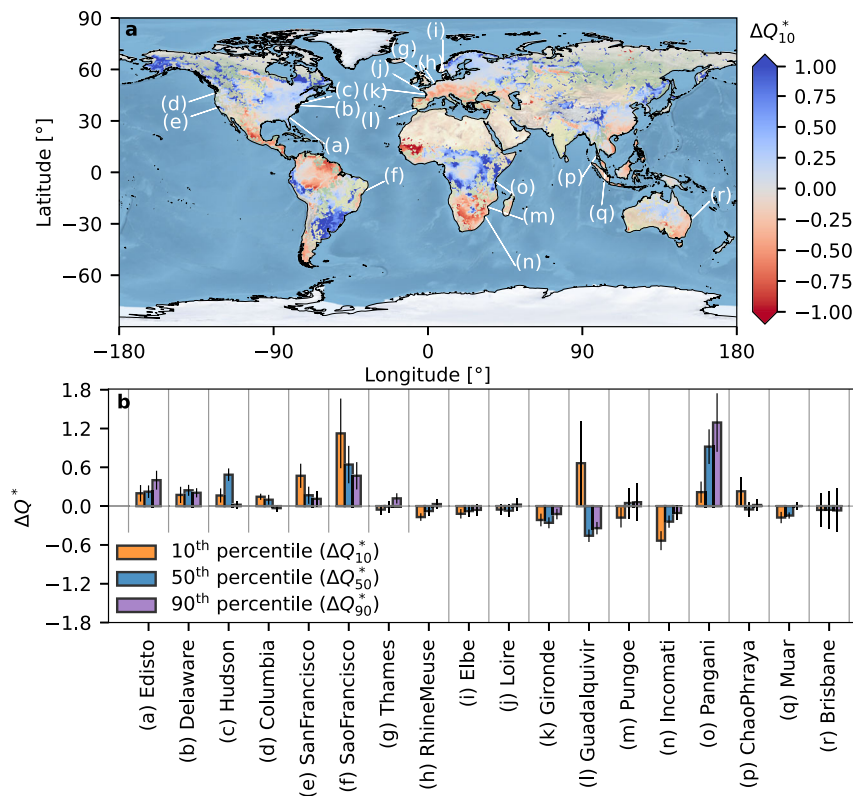
Fig. 1 | Future projections of river discharge under the Shared Socioeconomic Pathway (SSP) 3–7.0 in the Community Earth System Model 2 large ensemble simulations (CESM-LE2). a The relative changes in the 35-year mean low discharge (Q_{10}) for the future period (2066–2100) compared to present period (1996–2030), where the low discharge is defined as the annual 10th percentile of river discharge. The relative changes in Q_{10} correspond to $\Delta Q_{10}^* = (Q_{10}^f - Q_{10}^p)/Q_{10}^p$, where Q_{10}^p and Q_{10}^f are the time-averaged Q_{10} over present (1996–2030) and future (2066–2100) periods. Blue and red areas show projected increase and decrease of Q_{10} in future, respectively. Grid cells containing $Q_{10}^p < 1\,\mathrm{m^3 s^{-1}}$ are masked. The basemap is from Natural Earth. **b** The relative changes in the 10th (orange), 50th (blue), and 90th (purple) percentile of the 35-year mean river discharge between future and present periods, expressed by different subscripts in Q. Here the vertical solid black lines show the ensemble standard deviation of the projected river discharge in CESM-LE2. In both panels, positive and negative ΔQ^* are associated with projected decrease and increase of salt intrusion length in the future period.

and tide gauges (Methods). The projected VLM accounts for Glacial Isostatic Adjustment (GIA), subsidence due to acquifer withdrawal, and tectonic movements, among many others. Fig. 2b presents changes in water depth due to VLM, where positive values (blue) indicate land uplift (which decreases RSLR), while negative values (red) represent land sinking (which increases RSLR). The land uplift in Canada and northern Europe is attributed to GIA rebound, while the land subsidence in East coast of US and western Europe is mainly associated with the GIA forebulge collapse[27,33]. Fig. 2c shows the contributions of ASLR and VLM to changes in the 35-year mean of water surface elevation for the selected estuaries. The temporal evolution of RSLR processes to changing water depth for each estuary is provided in Supplementary Fig. S5 and S6. For all the studied estuaries, steric expansion is the dominant contributor to increasing water surface elevation. For most estuaries, contributions from Glaciers and Antarctica are the second and third largest, while contributions from Greenland is less significant. We find that VLM contributions to δH_R are less than 15% except for the US coast and Thailand.

Salt intrusion length projections

With the quantified changes in future river discharge and RSLR, we computed salt intrusion length for the selected estuaries using a 2DV salt intrusion model (Methods)[34]. The salt intrusion model accounts for along-estuary varying width, and assumes a flat channel bed (Supplementary Fig. S7). Measured along-estuary salinity profiles were used to calibrate the salt intrusion model. The root mean square error of the calibrated model ranges from 0.56 to 3.63 psu (median = 1.22 psu, see

Supplementary Fig. S8). The relative changes in the 35-year mean of annual salt intrusion length statistics are presented in Fig. 3a (the 90th percentile, ΔX_{90}^*) and Fig. 3b (the 50th percentile, ΔX_{50}^*) under four different combinations among dominant forcing agents. The relative changes in salt intrusion length are defined as $\Delta X_{pct}^* = (X_{pct}^f - X_{pct}^p)/X_{pct}^p$, where the superscript p and f represent the present (1996–2030) and future (2066–2100) periods, and the subscript pct denotes the percentile. The four sets of simulations consider (1) only river discharge changes (δQ), (2) only ASLR (δH_A), (3) only RSLR (δH_R), and (4) both river discharge changes and RSLR (δQ & δH_R). Fig. 3 shows that salt intrusion decreases (ΔX_{90}^* and $\Delta X_{50}^* < 0$) due to increased river discharge in the selected estuaries in the North and South America, and East Africa. For the rest of the studied estuaries, salt intrusion increases (ΔX_{90}^* and $\Delta X_{50}^* > 0$) because of the reduced river discharge. Ranges of the effects of future river discharge on the relative salt intrusion length are $-0.41 \leq \Delta X_{90}^* \leq 0.10$ (median = -0.002) and $-0.36 \leq \Delta X_{50}^* \leq 0.28$ (median = 0.01). We find that the magnitude of relative increases in salt intrusion length due to changes in river discharge in this study are smaller as compared to values reported in an earlier study[18] for western and southern Europe. The differences originate from the fact that, here, we use a more advanced salt intrusion model that is capable of accounting for converging estuary width. The salt intrusion model is less sensitive to changes in river discharge when using converging estuary width in the along-estuary direction.

The salt intrusion length consistently increases due to ASLR, as an increase in water depth enhances salt intrusion, ranging from
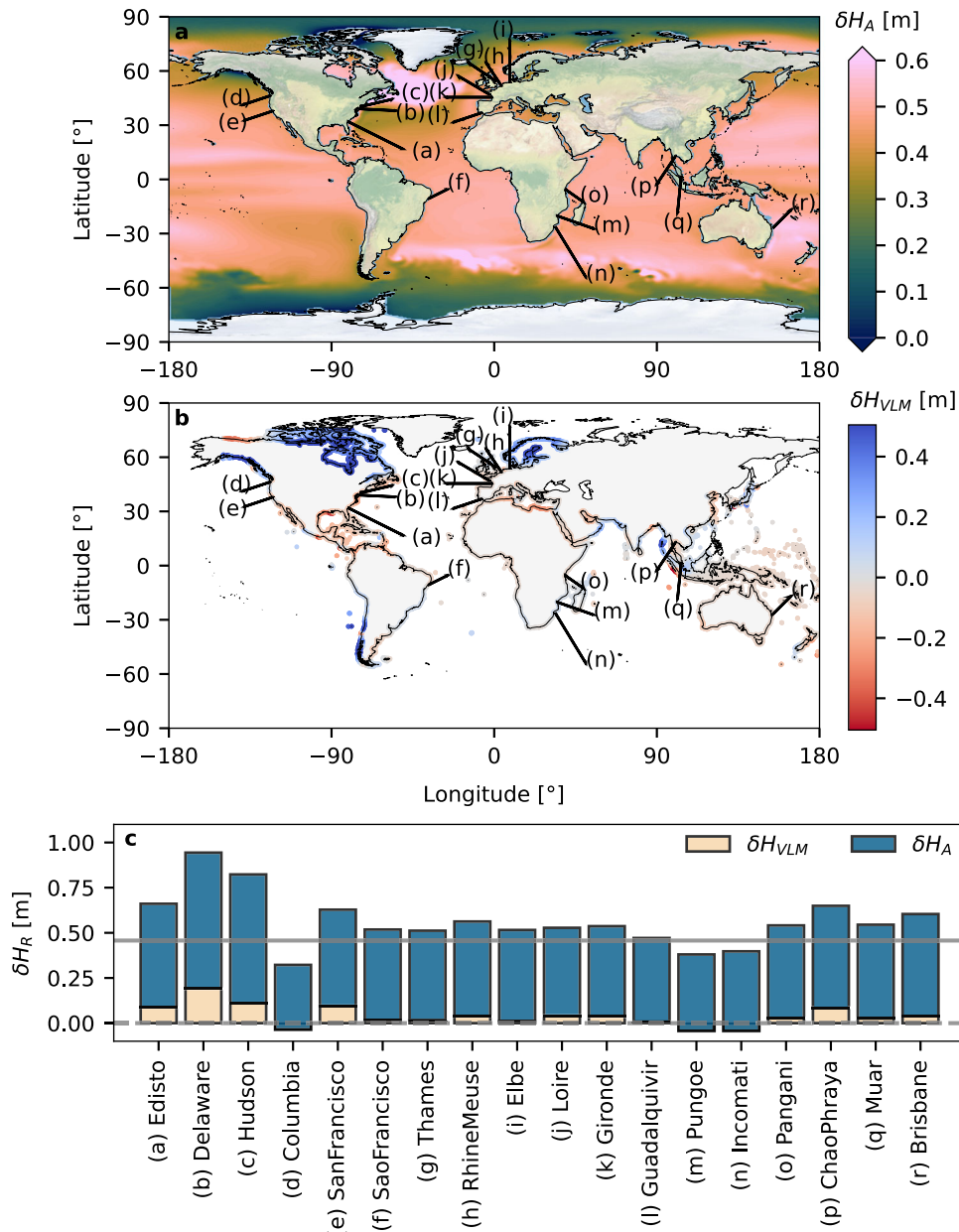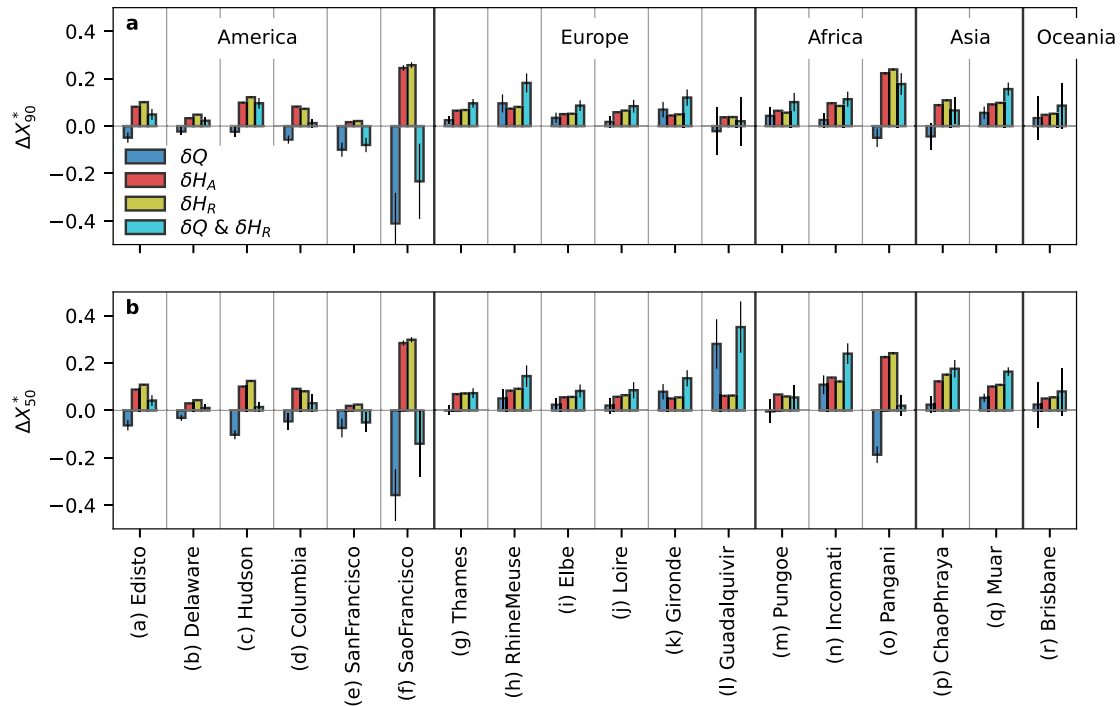
Fig. 2 | Future projections of total sea-level rise under the Shared Socio-economic Pathway (SSP) 3-7.0. a Absolute changes of the 35-year mean of water surface elevation between future (2066–2100) and present (1996–2030), δH_A. **b** Changes in water depth due to vertical land motion along global coastlines δH_{VLM}. In **a** and **b**, the basemap is from Natural Earth. **c** Contributions of δH_A and δH_{VLM} to the changes in water depth due to relative sea-level rise for each estuary δH_R. The horizontal gray solid and dashed lines show the global mean sea-level rise averaged in the future (2066–2100) and zero, respectively.

$0.017 \le \Delta X^*_{90} \le 0.25$ (median = 0.069) and $0.019 \le \Delta X^*_{50} \le 0.28$ (median = 0.076). By including the VLM, future salt intrusion increases range from $0.021 \le \Delta X^*_{90} \le 0.26$ (median = 0.071) and $0.024 \le \Delta X^*_{50} \le 0.30$ (median = 0.076). The result indicates that the contribution of VLM to changes in future salt intrusion length is insignificant. We find that the effect of RSLR on future salt intrusion length exceeds that due to changes in river discharge. This holds when we consider only estuaries with increasing ΔX^*_{90} due to the reduced magnitude of low discharge (estuaries: g–k, m, n, q, r). For those estuaries, changes in salt intrusion lengths are $0.018 \le \Delta X^*_{90} \le 0.096$ (median = 0.035) and $0.049 \le \Delta X^*_{90} \le 0.098$ (median = 0.066) when isolated δQ and δH_R are considered, respectively. Our analysis of the decomposed contributions of future forcing highlights the importance of RSLR on increasing salt intrusion length at the end of the 21st century. Compound changes in river discharge and RSLR (δQ & δH_R

case) lead to $-0.23 \le \Delta X^*_{90} \le 0.18$ (median = 0.079) and $-0.15 \le \Delta X^*_{50} \le 0.35$ (median = 0.072).

We further computed changes in the return periods and levels of extreme salt intrusion events. We first calculated return periods and levels using the 35-year annual maximum timeseries X^A_{max} for the present and future periods (the triangle and circle markers in Fig. 4a). Next, Generalized Extreme Value (GEV) distribution functions were fitted to the return period curves for each period (gray dashed and orange solid lines for present and future). Here, 100-year events were considered as typical extreme events (blue vertical line). The extreme return levels were defined as extrapolated X^A_{max} that corresponds to the 100-year return periods based on the fitted GEV distribution functions (i.e., X^A_{max} where gray dashed and orange solid curves intersect with the vertical blue line). The extreme return levels for the present and future are denoted as X^{yr100}_p and X^{yr100}_f, respectively (red

Fig. 3 | Future projections of surface water salt intrusion length under the Shared Socioeconomic Pathway (SSP) 3-7.0. a Relative changes of the 35-year mean of annual 90th percentile salt intrusion length between the future (2066–2100) and present (1996–2030) periods. Four combinations among the considered forcing agents are investigated: (1) only river discharge changes (δQ), (2) only absolute sea-level rise is imposed (δH_A), (3) only relative sea-level rise is imposed (δH_R), and (4) both river discharge changes and relative sea-level rise are considered ($\delta Q \& \delta H_R$). The vertical black solid lines represent one ensemble standard deviation from different realizations of climate conditions in the Community Earth System Model 2 large ensemble simulations (CESM-LE2). **b** The same as **a**, but for relative changes of 35-year mean of annual 50th percentile salt intrusion length. In both panels, positive and negative ΔX^* show projected increase and decrease of salt intrusion length in the future period.
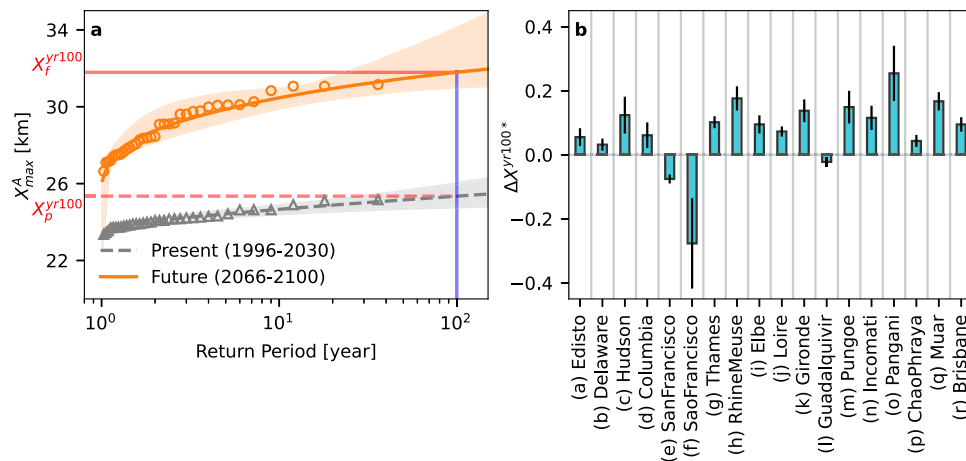
Fig. 4 | Projected changes in 100-year return levels when all the future forcings are considered, including changes in river discharge and relative sea-level rise, $\delta Q \& \delta H_R$ case. a An example of return periods and levels computed from the 35-year annual maximum timeseries X_{max}^A for Pangani (Tanzania) for present (1996–2030) and future (2066–2100). Here, gray triangles and orange circles show estimated return periods. The corresponding gray dashed and orange solid lines are the fitted curves using the generalized extreme value distribution function. The shaded areas present 95% confidence interval computed by the bootstrapping method. The blue vertical line demarks the 100-year return period, defined as an extreme event. The horizontal red dashed and solid lines represent return levels corresponding to the extreme events for the present (X_p^{yr100}) and future (X_f^{yr100}), respectively. The same plots for all the studied estuaries are presented in Supplementary Fig. S9. **b** The relative changes of the future extreme return levels, $\Delta X^{yr100*} = (X_f^{yr100} - X_p^{yr100})/X_p^{yr100}$. The vertical black solid lines show uncertainties associated with 95% confidence interval using the bootstrapping method.

horizontal dashed and solid lines, respectively). Pangani was taken as an example to visualize the changes in return period curves where we observed the largest relative increases in the future 100-year return level (Fig. 4a). The same plots for all the remaining estuaries are presented in Supplementary Fig. S9. The relative changes of the 100-year return levels are defined as $\Delta X^{yr100*} = (X_f^{yr100} - X_p^{yr100})/X_p^{yr100}$. The following results focus only on the future simulations in which all the changes in forcings are considered, including the river discharge and RSLR ($\delta Q \& \delta H_R$ case). We find $-0.28 \le \Delta X^{yr100*} \le 0.25$ (median 0.095) for all the studied estuaries and $0.032 \le \Delta X^{yr100*} \le 0.25$ (median 0.10)

for the 83% of the estuaries (15 out of 18) showing increasing future 100-year return levels. The changed future return periods for the extreme events were computed by finding points where X_p^{yr100} intersect with future return curves (i.e., the red horizontal dashed lines meet with the orange solid lines in Fig. 4a). It is found that such future return periods are projected to decrease to 3.2 years for 6 estuaries on average (a,b,d,n,p,r in Supplementary Fig. S9). For 9 estuaries (c,g–k,m,o,q in Supplementary Fig. S9), the salt intrusion length belonging to a future 2-year return level is larger than ones corresponding to the extreme event under present-day conditions, as is seen from the orange circles always being above the red horizontal dashed lines. For 3 estuaries (e,f,l in Supplementary Fig. S9), return levels in future are projected to be reduced because of increasing magnitude of low discharge. Our results show that events that are considered as extreme in the present-day would occur much more frequent under changes in river discharge and increasing water depth in the future climate.

Discussion

Our analysis provides future projections of the global-scale salt intrusion length under the high emission scenario (SSP3-7.0) using CESM-LE2 with two dominant future forcing agents: river discharge and RSLR. We show that the 35-year mean annual 90th percentile salt intrusion length is projected to range from 1.3% to 18.2% (median 9.1%) in 89% of the studied estuaries (16 out of 18). We also quantify that return levels of 100-year events are intensified in the future by 3.2–25.2% (median 10.2%) in 83% of the studied estuaries (15 out of 18). A systematic decomposition of the effects of changes in river discharge and water depth on future salt intrusion length allows to investigate the relative importance of the two forcings. We find that increasing water depth due to RSLR and decreasing river discharge are responsible for increasing salt intrusion length from 4.9% to 9.6% (median 6.6%) and from 1.7% to 9.6% (median 3.5%), respectively. This indicates that increasing water depth due to RSLR contributes to increasing future salt intrusion length approximately twice as much than decreasing river discharge. We stress that the factor two greater contribution by RSLR is from averaged salt intrusion length simulation results among the studied estuaries, and the relative importance of each forcing can vary significantly.

To better understand why our simulation results show greater contributions from elevating water depth to increasing salt intrusion length, we examined this based on the reduced-complexity steady state tidally-averaged salt budget equation (Eq. S14)[35–38]. As shown in Supplementary Note S2, salt intrusion length scales as $X \sim H^m Q^n$. Here, $m = 2$ and $n = -1/3$ for stratified estuaries (exchange flow dominant regime, Eq. S17), while $m = 1$ and $n = -1$ for well-mixed estuaries (tidal dispersion dominant regime, Eq. S19), respectively. These scaling relations highlight that X is six times more sensitive to changes in H as compared to changes in Q ($|m/n| = 6$) for stratified estuaries. For well-mixed estuaries, X similarly responds to changes in H and Q ($|m/n| = 1$). This implies that X is expected to respond 1-6 times more sensitively to changes in H as compared to changes in Q for partially-mixed estuaries. As seen in Fig. S10, most of the studied estuaries are classified as partially-mixed estuaries (Supplementary Note 3 and Fig. S10).

The increased mean and extreme surface water salt intrusion length are expected to pose significant socio-economic challenges in coastal regions in the coming decades. For instance, when saline ocean water intrudes more frequently farther upstream, freshwater intakes are more likely to be contaminated. Increases in salinity and an extended salt intrusion length can affect agricultural landscape, reducing crop yields or forcing farmers to grow salt-tolerant species[17]. In addition, a higher drinking water salinity has been shown to elevate the risks of cardiovascular and kidney health problems[39]. Failure to adapt to these new agricultural conditions in a timely manner can lead to substantial economic loss and food shortage[17]. Our findings imply

that these surface water salinization problems are projected to worsen in many estuaries worldwide.

Although our study provided a global-scale view on how changing water depth and river discharge affect salt intrusion, further improvements can be made for future projections. Incorporating realistic bottom topography will be an important step forward in capturing local estuarine dynamics and salt intrusion processes. When the water depth is increased, inhomogeneous residual circulation patterns emerge depending on the bathymetric characteristics[40]. This modulated residual circulation can influence local salt transport and salt intrusion length. Furthermore, the rate of local sedimentation build-up and erosion due to future coastal and fluvial morphodynamics can be characterized[41]. With this additional contribution, we can better quantify the effective change of water depth in estuaries. In addition, anthropogenic water regulation (e.g., reservoir operation and water withdrawal) is a significant source of uncertainties for projections of river discharge and salt intrusion. Changing dynamics of tides[10], winds[13], and ocean salinity[12] in estuaries can play a role in future salt intrusion by influencing mixing and stratification.

The proposed framework in this study can be applied to any other estuaries if essential observations for the analysis are available: estuary geometries, longitudinal salinity measurements, multi-year daily river discharge data from observation, and reliable modeled river discharge from a climate model. We acknowledge that our analysis focuses on relatively large mid-latitude estuaries, where all the necessary data are publicly accessible. To provide a more comprehensive view of future salt intrusion processes in other estuaries, collective efforts to make necessary salinity and hydrological data publicly available will be crucial. Such data-sharing efforts with additional modeling work can help better understand future salt intrusion processes that are not addressed in this study, such as those occurring in fjords.

Methods
CESM
CESM is a fully coupled global climate model simulating ocean, land, atmospheric, and sea-ice processes, and their feedbacks. In this study, we projected future river discharge and sea-level rise under the SSP3-7.0 based on the CESM2 large ensemble simulation results, CESM-LE2 ($n = 69$). Here n is the total number of ensemble members considered, where consistent data are publicly available for daily river discharge, monthly air surface temperature, and monthly precipitation. The SSP3-7.0 represents the medium to high end of emission scenario, proposed in the Coupled Model Intercomparison Project Phase 6 (CMIP6). Following priority protocols in CMIP6, CESM-LE2 focused on the SSP3-7.0 due to large computational costs. A nominal horizontal spatial resolution of 1° was used for periods 1850–2100 in all the simulations. The SSP3-7.0 forcing scenario was applied from the year 2015. More detailed descriptions of CESM-LE2 are documented at https://www.cesm.ucar.edu/community-projects/lens2[42].

River discharge
The modeled daily river discharge consists of contributions from surface and groundwater, and ice melt runoff computed in the land surface model in CESM-LE2. The accumulated total runoff on the land surfaces is routed to river networks with spatially varying river flow velocities using Manning's equation, based on heterogeneous roughness, hydraulic radius, and water surface slopes in land grid cells[43,44]. The modeled river discharge is abstracted depending on irrigation demands in land grid cells, but flow regulations by reservoirs are not considered[45]. We adjusted systematic biases observed in the modeled river discharge using the Quantile Delta Mapping (QDM) method[25]. The QDM method that was used to correct the modeled river discharge is elaborated in detail in ref. 18 (Supplementary Note S1 therein). Comparisons between seasonally averaged river discharge from CESM-LE2 and observations (before and after the bias correction)

are provided in Supplementary Fig. S1. Changes of the seasonally averaged river discharge in CESM-LE2 between present (1996–2030) and future (2066–2100) are also given in Supplementary Fig. S2. Locations and measurement periods of the observed river discharge are summarized in Supplementary Table S1.

Absolute sea-level rise (ASLR)

Future sea-level rise (2066–2100) was projected by post-processing the modeled air surface and oceanic temperature, and snowfall results in CESM-LE2, following the methods outlined in ref. [26]. In these methods, the global mean sea-level rise (GMSLR) consists of four major contributions: (1) steric expansion, and ice melt from the (2) Antarctica and (3) Greenland ice sheets as well as (4) glaciers. Here, the steric expansion was quantified by vertically integrating specific volume anomalies over the full depth of the water column[46], which is associated with volume expansion of the water column due to changes in density by varying temperature, pressure, and salinity. The SLR due to the melting Antarctica ice sheet was calculated based on surface mass balance[47] and basal melt[48], using snowfall over the continent and oceanic temperatures adjacent to the continental shelves. The contribution by the Greenland ice sheet was computed based on a mass balance between snowfall and surface melt[49]. The contribution by the glaciers was calculated using power law relations between sea-level rise and global mean surface temperature anomalies[47]. Nineteen glacier regions in the Randolph Glacier Inventory were considered, excluding glaciers in the Antarctica and sub-Antarctica regions.

Because we projected future salt intrusion length for estuaries at the global scale, it was crucial to consider spatial variability in the sea-level rise projection. Two sources of spatial variability were quantified in our analysis. First, we computed Gravitational, Rotational, and Deformation (GRD) effects induced by decreasing ice mass[50]. The GRD effects are induced by reduced gravitational force due to decreased ice mass that pulls water surface, resulting in greater SLR away from ice melting sources (Supplementary Fig. S3). Second, we also characterized spatial patterns in changes of dynamic sea-level changes (DSL) that are associated with varying regional wind stresses and large-scale ocean circulations over the 21st century (Supplementary Fig. S4). Decadal changes of DSL are calculated based on a climate model output (variable name *SSH*) in CESM-LE2. Temporal evolution of different contributors to ASLR for each estuary is provided in Supplementary Fig. S5.

We assumed that SLR processes are relatively slow as compared to changes in daily river discharge. To create consistent temporal resolution of SLR as daily river discharge, we linearly interpolated annual ASLR due to steric expansion and ice melt with GRD as well as monthly DSL into daily changes.

Vertical land motion (VLM)

To quantify relative sea-level changes, we employed projected VLM along global coastlines that is presented in ref. [27]. Therein, VLM was reconstructed from 1995 to 2020 by combining direct VLM observation from Global Navigation Satellite Systems (GNSS)[51] and an indirect VLM predictions that are based on tide gauges[52] and altimetry data. Potential nonlinear VLM processes (e.g. glacial isostatic adjustment, tectonic activity, surface mass loading changes, and local natural or anthropogenic effects) were considered in space and time in the reconstruction. The quantified statistical properties of VLM trends and uncertainties in the reconstruction were used to project VLM up to the year 2150[27]. Changes in water depth due to VLM are presented along global coastlines in Fig. 2b. The temporal evolution of VLM up to the year 2100 is shown for each investigated estuary in Supplementary Fig. S6. Similar to ASLR, we linearly extrapolated the VLM trends into daily-scale changes.

Estuary geometries

In this study, we assumed uniform water depth, allowing along-estuary varying width from the mouth to inland. To construct the converging

estuary width, we fitted an exponential function to directly measured data in field campaigns[53] and Google Earth[34]. For estuaries, in which width data was unavailable from the literature, we employed remotely sensed data from satellite images (Global River Widths from Landsat, GRWL)[54]. We divided estuaries into segments, where the index i is an integer, numbering the segments. The index $i = 0$ is the estuary segment adjacent to the mouth and increasing i indicates segments away from the mouth to inland. The equation for the estuary width of each segment reads

$$\begin{cases} B(x) = B_{s,i} \exp(x/L_{c,i}) & \text{for } i = 0, \\ B(x) = B_{s,i} \exp((x + L_{s,i-1})/L_{c,i}) & \text{for } i \geq 1. \end{cases} \quad (1)$$

Here, x is the along-estuary coordinate with the origin $x = 0$ at the estuary mouth and negative upstream. The constant coefficients $B_{s,i}$, $L_{s,i}$, and $L_{c,i}$ represent the largest estuary width facing seaward, streamwise estuary length, and convergence length at each segment, respectively. The characteristics of estuary geometries used in our analysis are summarized in Supplementary Table S2. Comparisons between the observed estuary width and Eq. (1) are provided in Supplementary Fig. S7.

Salt intrusion model

We computed two-dimensional salinity structures in the along-estuary and vertical coordinates (2DV) using a time-dependent, width and tidally averaged single channel salt intrusion model. The 2DV salt intrusion model solves the mass, momentum, and salt balances with parameterized horizontal and vertical eddy viscosity and diffusivity[34,55]. The salt balance describes the temporal changes in salinity due to seaward salt flux caused by advection by river flow and landward salt flux by density driven exchange flow and horizontal mixing induced by tidal disperson. The solution methods for the 2DV salt intrusion model are given in ref. [34] and Supplementary Note S1.

We ran spin-up simulations for 1 year for the present (the year 1995) and future (the year 2065). Next, we conducted simulations for 35 years in the periods 1996–2030 (present) and 2066–2100 (future) using time series of river discharge, SLR, and VLM. The effects of changes in river discharge and RSLR on salt intrusion length at the end of the 21st century were systematically investigated by switching on/off future forcings. When considering changes in river discharge alone (blue vertical bar, δQ in Fig. 3), we used river discharge time series from 1996–2030 and 2066–2100 for the present and future periods, while imposing ASLR time series from 1996–2030 for both periods. When examining the impact of ASLR only (red vertical bar, δH_A in Fig. 3), we employed the ASLR time series from 1996–2030 and 2066–2100 for the present and future periods, while using river discharge time series from 1996–2030 for both periods. For VLM contributions, we added VLM to ASLR timeseries (yellow vertical bar, δH_R in Fig. 3). To analyze the combined contributions of river discharge and RSLR to future salt intrusion length (cyan vertical bar, δQ & δH_R in Fig. 3), we used river discharge and RSLR timeseries from 1996–2030 and 2066–2100 for the present and future periods, respectively.

Model calibration

Salinity measurements were available in different time scales, which were needed for the model calibration. First, we utilized one-day snapshots of salinity field $s(x)$ collected during dry seasons. Second, we used salinity timeseries measured at multiple spatial locations $s(x, t)$ with daily (or monthly) temporal resolutions (Supplementary Table S4). For consistent model calibration, if applicable, we used time-averaged longitudinal salinity profiles over the month when the seasonally averaged river discharge is the lowest, denoted as $s_{dry}(x) = \langle s(x,t) \rangle_{dry}$. Here, $\langle \cdot \rangle$ is a time-averaging operator, and subscript *dry* indicates a period of interest, which was the driest month. The period of interest (dry seasons) was aligned with the purpose of our analysis to project changes in the potentially largest salt intrusion

length for the future. When the vertical locations of salinity measurements were inconsistent among the data sources, we assumed the data to represent the depth-averaged salinity fields. If salinity data were collected at one vertical location and the measurement depth was reported, we extracted salinity profiles from the 2DV salt intrusion model at the corresponding vertical locations for the calibration. If the information about the vertical measurement locations was inaccessible from the data sources, we assumed the salinity profiles were from surface measurements (1m below the water surface).

Two constants for horizontal eddy diffusivity c_h and vertical eddy viscosity c_v were used as primary calibrating parameters in the 2DV salt intrusion model. We generated 200 - 400 combinations of c_v and c_h using the stochastic gradient descent method[56]. These combinations of c_v and c_h allowed to obtain the minimum root mean square errors of longitudinal salinity profiles between observation and model results, while keeping the absolute difference between modeled and observed X minimal. It was ensured that values of the ensemble-averaged c_v and c_h were independent of the number of combinations. If the ocean boundary salinity s_{ocn}, which is a forcing parameter of the model, is not directly measured in observations, s_{ocn} was also determined together with c_v and c_h following the same procedure. The ensemble averaged c_v and c_h from the combinations were defined as the calibrated eddy viscosity and diffusivity parameters. The corresponding ensemble standard deviations were defined as uncertainties associated with 2DV salt intrusion model calibrations (Supplementary Table S3).

Data availability
All the data sources are given in Supplementary Table S4. The raw and processed data used and generated in this study have been deposited in Zenodo (https://doi.org/10.5281/zenodo.14837324). The basemap used in all figures in this paper is available at https://www.naturalearthdata.com/.

Code availability
All the scripts and raw and processed data that reproduce the figures in this paper have been deposited in Zenodo (https://doi.org/10.5281/zenodo.14837324).

References
1. Valle-Levinson, A., Contemporary Issues in Estuarine Physics. Cambridge University Press, Cambridge, United Kingdom (2010).
2. Miller, P. & Hiatt, M. Hydrometeorological drivers of the 2023 Louisiana water crisis. *Geophys. Res. Lett.* **51**, 2024–108545 (2024).
3. Wullems, B. J., Brauer, C. C., Baart, F. & Weerts, A. H. Forecasting estuarine salt intrusion in the Rhine-Meuse delta using an LSTM model. *Hydrol. Earth Syst. Sci.* **27**, 3823–3850 (2023).
4. Naumann, G. et al. Global changes in drought conditions under different levels of warming. *G* **45**, 3285–3296 (2018).
5. Liu, W. et al. Global drought and severe drought-affected populations in 1.5 and 2 C warmer worlds. *Earth Syst. Dyn.* **9**, 267–283 (2018).
6. Ji, Y., Fu, J., Lu, Y. & Liu, B. Three-dimensional-based global drought projection under global warming tendency. *Atmos. Res.* **291**, 106812 (2023).
7. Hong, B. & Shen, J. Responses of estuarine salinity and transport processes to potential future sea-level rise in the Chesapeake Bay. *Estuar. Coast. Shelf Sci.* **104**, 33–45 (2012).
8. MacCready, P. & Geyer, W. R. Advances in estuarine physics. *Annu. Rev. Mar. Sci.* **2**, 35–58 (2010).
9. Geyer, W. R. & MacCready, P. The estuarine circulation. *Annu. Rev. Fluid Mech.* **46**, 175–197 (2014).
10. Pickering, M. et al. The impact of future sea-level rise on the global tides. *Cont. Shelf Res.* **142**, 50–68 (2017).
11. Matsoukis, C., Amoudry, L. O., Bricheno, L. & Leonardi, N. Numerical investigation of river discharge and tidal variation impact on salinity

12. intrusion in a generic river delta through idealized modelling. *Estuaries Coasts* **46**, 57–83 (2023).
12. Lee, Y. J. & Lwiza, K. M. Factors driving bottom salinity variability in the Chesapeake Bay. *Cont. Shelf Res.* **28**, 1352–1362 (2008).
13. Jongbloed, H., Schuttelaars, H. M., Dijkstra, Y. M., Donkers, P. B. & Hoitink, A. J. Influence of wind on subtidal salt intrusion and stratification in well-mixed and partially stratified estuaries. *J. Phys. Oceanogr.* **52**, 3139–3158 (2022).
14. Bellafiore, D. et al. Saltwater intrusion in a Mediterranean delta under a changing climate. *J. Geophys. Res.: Oceans* **126**, 2020–016437 (2021).
15. Zhu, J. et al. Dynamic mechanism of an extremely severe saltwater intrusion in the Changjiang Estuary in February 2014. *Hydrol. Earth Syst. Sci.* **24**, 5043–5056 (2020).
16. Jassby, A. D. et al. Isohaline position as a habitat indicator for estuarine populations. *Ecol. Appl.* **5**, 272–289 (1995).
17. Loc, H. H. et al. How the saline water intrusion has reshaped the agricultural landscape of the Vietnamese Mekong Delta, a review. *Sci. Total Environ.* **794**, 148651 (2021).
18. Lee, J., Biemond, B., de Swart, H. & Dijkstra, H. A. Increasing risks of extreme salt intrusion events across European estuaries in a warming climate. *Commun. Earth Environ.* **5**, 60 (2024).
19. Bhuiyan, M. J. A. N. & Dutta, D. Assessing impacts of sea-level rise on river salinity in the Gorai river network, Bangladesh. *Estuar., Coast. Shelf Sci.* **96**, 219–227 (2012).
20. Chua, V. P. & Xu, M. Impacts of sea-level rise on estuarine circulation: An idealized estuary and San Francisco Bay. *J. Mar. Syst.* **139**, 58–67 (2014).
21. Krvavica, N. & Ružić, I. Assessment of sea-level rise impacts on salt-wedge intrusion in idealized and Neretva River Estuary. *Estuar., Coast. Shelf Sci.* **234**, 106638 (2020).
22. Yang, Z., Wang, T., Voisin, N. & Copping, A. Estuarine response to river flow and sea-level rise under future climate change and human development. *Estuar., Coast. Shelf Sci.* **156**, 19–30 (2015).
23. Rodrigues, M., Fortunato, A. B. & Freire, P. Saltwater intrusion in the upper Tagus Estuary during droughts. *Geosciences* **9**, 400 (2019).
24. Eslami, S. et al. Projections of salt intrusion in a mega-delta under climatic and anthropogenic stressors. *Commun. Earth Environ.* **2**, 142 (2021).
25. Cannon, A. J., Sobie, S. R. & Murdock, T. Q. Bias correction of GCM precipitation by quantile mapping: how well do methods preserve changes in quantiles and extremes? *J. Clim.* **28**, 6938–6959 (2015).
26. van Westen, R. M. & Dijkstra, H. A. Ocean eddies strongly affect global mean sea-level projections. *Sci. Adv.* **7**, 1674 (2021).
27. Oelsmann, J. et al. Regional variations in relative sea-level changes influenced by nonlinear vertical land motion. *Nat. Geosci.* **17**, 137–144 (2024).
28. van Vliet, M. T. Global river discharge and water temperature under climate change. *Glob. Environ. Change* **23**, 450–464 (2013).
29. Asadieh, B. & Krakauer, N. Y. Global change in streamflow extremes under climate change over the 21st century. *Hydrol. Earth Syst. Sci.* **21**, 5863–5874 (2017).
30. Stern, M. A., Flint, L. E., Flint, A. L., Knowles, N. & Wright, S. A. The future of sediment transport and streamflow under a changing climate and the implications for long-term resilience of the San Francisco Bay Delta. *Water Resour. Res.* **56**, 2019–026245 (2020).
31. Bouttes, N., Gregory, J. M., Kuhlbrodt, T. & Smith, R. The drivers of projected North Atlantic sea-level change. *Clim. Dyn.* **43**, 1531–1544 (2014).
32. Palmer, M. et al. Exploring the drivers of global and local sea-level change over the 21st century and beyond. *Earth's Future* **8**, 2019–001413 (2020).
33. Hammond, W. C., Blewitt, G., Kreemer, C. & Nerem, R. S. GPS imaging of global vertical land motion for studies of sea-level rise. *J. Geophys. Res. Solid Earth* **126**, 2021–022355 (2021).

34. Biemond, B., de Swart, H. E., Dijkstra, H. A. & Dìez-Minguito, M. et al. Estuarine salinity response to freshwater pulses. *J. Geophys. Res.: Oceans* **127**, 1–18 (2022).

35. Monismith, S. G., Kimmerer, W., Burau, J. R. & Stacey, M. T. Structure and flow-induced variability of the subtidal salinity field in northern San Francisco Bay. *J. Phys. Oceanogr.* **32**, 3003–3019 (2002).

36. MacCready, P. Toward a unified theory of tidally-averaged estuarine salinity structure. *Estuaries* **27**, 561–570 (2004).

37. Chen, S.-N. Asymmetric estuarine responses to changes in river forcing: A consequence of nonlinear salt flux. *J. Phys. Oceanogr.* **45**, 2836–2847 (2015).

38. Ralston, D. K. & Geyer, W. R. Response to channel deepening of the salinity intrusion, estuarine circulation, and stratification in an urbanized estuary. *J. Geophys. Res.: Oceans* **124**, 4784–4802 (2019).

39. Xeni, C. et al. Epidemiological evidence on drinking water salinity and blood pressure: a scoping review. *Environ. Res.: Health* **1**, 035006 (2023).

40. Valentim, J. M. et al. Sea-level rise impact in residual circulation in Tagus estuary and Ria de Aveiro lagoon. *J. Coast. Res.* **65**, 1981–1986 (2013).

41. Hou, X., Xie, D., Feng, L., Shen, F. & Nienhuis, J. H. Sustained increase in suspended sediments near global river deltas over the past two decades. *Nat. Commun.* **15**, 3319 (2024).

42. Rodgers, K. B. et al. Ubiquity of human-induced changes in climate variability. *Earth Syst. Dyn.* **12**, 1393–1411 (2021).

43. Tesfa, T. K. et al. A subbasin-based framework to represent land surface processes in an Earth system model. *Geosci. Model Dev.* **7**, 947–963 (2014).

44. Li, H.-Y. et al. Evaluating global streamflow simulations by a physically based routing model coupled with the Community Land Model. *J. Hydrometeorol.* **16**, 948–971 (2015).

45. Taranu, S. I. et al. Bridging the gap: a new module for human water use in the Community Earth System Model version 2.2.1. *Geosci. Model Dev.* **17**, 7365–7399 (2024).

46. Richter, K., Riva, R. & Drange, H. Impact of self-attraction and loading effects induced by shelf mass loading on projected regional sea-level rise. *Geophys. Res. Lett.* **40**, 1144–1148 (2013).

47. Church, J.A. et al. Sea level change. Technical report, PM Cambridge University Press (2013).

48. Levermann, A. et al. Projecting Antarctica's contribution to future sea-level rise from basal ice shelf melt using linear response functions of 16 ice sheet models (LARMIP-2). *Earth Syst. Dyn.* **11**, 35–76 (2020).

49. Fettweis, X. et al. Estimating the Greenland ice sheet surface mass balance contribution to future sea-level rise using the regional atmospheric climate model MAR. *Cryosphere* **7**, 469–489 (2013).

50. Frederikse, T., Landerer, F. W. & Caron, L. The imprints of contemporary mass redistribution on local sea-level and vertical land motion observations. *Solid Earth* **10**, 1971–1987 (2019).

51. Blewitt, G., Kreemer, C., Hammond, W. C. & Gazeaux, J. MIDAS robust trend estimator for accurate GPS station velocities without step detection. *J. Geophys. Res.: Solid Earth* **121**, 2054–2068 (2016).

52. Holgate, S. J. et al. New data systems and products at the permanent service for mean sea-level. *J. Coast. Res.* **29**, 493–504 (2013).

53. Gisen, J., Savenije, H. & Nijzink, R. Revised predictive equations for salt intrusion modelling in estuaries. *Hydrol. Earth Syst. Sci.* **19**, 2791–2803 (2015).

54. Allen, G. H. & Pavelsky, T. M. Global extent of rivers and streams. *Science* **361**, 585–588 (2018).

55. MacCready, P. Estuarine adjustment. *J. Phys. Oceanogr.* **37**, 2133–2145 (2007).

56. Kiefer, J., Wolfowitz, J. Stochastic estimation of the maximum of a regression function. *Ann. Math. Stat* **23**, 462–466 (1952).

Acknowledgements

Author contributions

J.L. designed the study, analyzed the main results, and led the writing of the paper. B.B. contributed to salt intrusion modeling analysis and reviewed the paper. D.v.K. contributed to creating estuary geometry data. Y.H. contributed to discussions and reviewed the paper. R.v.W. contributed to the sea-level rise projection analysis and reviewed the paper. H.de.S. designed the study and contributed to data analysis, and reviewed the paper. H.A.D. provided financial support and computational resources, designed the study, contributed to data analysis, and reviewed the paper. W.K. contributed to conceptualizing the study and reviewed the paper.

Competing interests

The authors declare no competing interests.

Additional information

Supplementary information The online version contains supplementary material available at https://doi.org/10.1038/s41467-025-58783-6.

Correspondence and requests for materials should be addressed to Jiyong Lee.

Peer review information *Nature Communications* thanks Christian Ferrarin, Braulio Juárez and the other, anonymous, reviewer(s) for their contribution to the peer review of this work. A peer review file is available.

Reprints and permissions information is available at http://www.nature.com/reprints

Publisher's note Springer Nature remains neutral with regard to jurisdictional claims in published maps and institutional affiliations.